PAPER

Check for updates

In situ-polymerized lithium salt as a polymer electrolyte for high-safety lithium metal batteries†

Shenghang Zhang, [abch] Fu Sun, [a] Xiaofan Du, [a] Xiaohu Zhang, [a] Lang Huang, [a] Jun Ma, [a] Shanmu Dong, [ai] André Hilger, [d] Ingo Manke, [d] Longshan Li, [a] Bin Xie, [a] Jiedong Li, [a] Zhiwei Hu, [e] Alexander C. Komarek, [e] Hong-Ji Lin, [f] Chang-Yang Kuo, [fg] Chien-Te Chen, [f] Pengxian Han, [a] Gaojie Xu, [*abci] Zili Cui [*abc] and Guanglei Cui [*abchi]

Polymer electrolytes offer advantages of leak-proofing, excellent flexibility, and high compatibility with lithium metal, enabling the highly safe operation of lithium metal batteries (LMBs). However, most current polymer electrolytes do not meet the requirements for the practical applications of LMBs. Herein, to resolve this issue, employing thermal-induced *in situ* polymerization of lithium perfluoropinacolatoaluminate (LiFPA), we present a novel interface-compatible and safe single-ion conductive 3D polymer electrolyte (3D-SIPE-LiFPA). It is demonstrated that 3D-SIPE-LiFPA with a unique polyanion structure promoted the formation of a protective electrode/electrolyte interface and inhibited the dissolution–migration–deposition of transition metals (TMs). 3D-SIPE-LiFPA endowed $LiNi_{0.8}Co_{0.1}Mn_{0.1}O_2$ (NCM811, 3.7 mA h cm^{-2})/Li (50 μm) LMBs with a long cycle life at both the coin-cell level (80.8% after 236 cycles) and pouch-cell level (437 W h kg^{-1}, 95.4% after 60 cycles, injected electrolyte 2 g A h^{-1}). More importantly, pouch-type NCM811/Li LMBs using 3D-SIPE-LiFPA delivered significantly enhanced onset temperature for heat release (T_{onset}) and thermal runaway temperature (T_{tr}) by 34 °C and 72 °C, respectively. Our strategy of polymerizing lithium salt as a polymer electrolyte opens up a new frontier to simultaneously enhance the cycle life and safety of LMBs.

Broader context

The gravimetric energy density of large-format pouch-type lithium metal batteries (LMBs) can exceed 500 W h kg^{-1} and has great potential to overcome the endurance mileage anxiety of electric vehicles. Nevertheless, the hitherto reported LMBs under practical conditions always suffer from poor cycle life and safety concerns, compared to conventional lithium-ion batteries (LIBs). Polymer electrolytes offer advantages of leak-proofing, excellent flexibility, and high compatibility with lithium metal. However, the hitherto reported polymer electrolytes constructed by *ex situ* or *in situ* methods cannot meet the requirements for the practical applications of LMBs. In this work, unprecedentedly through the *in situ* solidification of lithium salt anion (LiFPA), a single-ion polymer electrolyte (SIPE) with a 3D network (3D-SIPE-LiFPA) is successfully prepared. The as-prepared 3D-SIPE-LiFPA with a unique polyanion structure enables the construction of practical $LiNi_{0.8}Co_{0.1}Mn_{0.1}O_2$ (NCM811)/Li and high-voltage $LCoO_2$/Li batteries with long cycling stability and high thermal safety under extreme conditions. Our work sets a precedent of polymerizing lithium salt anions as polymer electrolyte, which will guide future polymer electrolyte innovations in both LMBs and LIBs.

[a] *Qingdao Industrial Energy Storage Research Institute, Qingdao Institute of Bioenergy and Bioprocess Technology, Chinese Academy of Sciences, No. 189 Songling Road, Qingdao 266101, China. E-mail: xugj@qibebt.ac.cn, cuizl@qibebt.ac.cn, cuigl@qibebt.ac.cn*

[b] *Shandong Energy Institute, Qingdao 266101, China*

[c] *Qingdao New Energy Shandong Laboratory, Qingdao 266101, China*

[d] *Helmholtz-Zentrum Berlin für Materialien und Energie, Hahn-Meitner-Platz 1, 14109 Berlin, Germany*

[e] *Max Planck Institute for Chemical Physics of Solids, Dresden, Germany*

[f] *National Synchrotron Radiation Research Center, Hsinchu, Taiwan 30076, Republic of China*

[g] *Department of Electrophysics, National Yang Ming Chiao Tung University, Hsinchu 30010, Taiwan, Republic of China*

[h] *School of Future Technology, University of Chinese Academy of Sciences, Beijing 100049, China*

[i] *Center of Materials Science and Optoelectronics Engineering, University of Chinese Academy of Sciences, Beijing 100049, China*

† Electronic supplementary information (ESI) available. See DOI: **https://doi.org/10.1039/d3ee00558e**

1. Introduction

To reach the battery goal of 500 W h kg^{-1}, lithium metal batteries (LMBs) consisting of an ultrathin Li anode (≤ 50 μm, 3860 mA h g^{-1}) and high areal capacity cathode (≥ 3.5 mA h cm^{-2}, such as nickel-rich layered LiNi$_x$Co$_y$Mn$_{1-x-y}$O$_2$, NCM, $x + y + z = 1$, $x \geq 0.8$) are promising candidates.[1–5] However, parasitic reactions between the Li anode and electrolytes will cause a series of severe problems, such as Li dendrites growth and Li anode pulverization, deteriorating the safety and cycle life of LMBs.[6–9] Moreover, the Li anode stability issue can be exacerbated by an uncontrollable cross-talking of the byproducts from the cathode/electrolyte reactions.[7,10] To resolve these issues, representative strategies, such as liquid electrolyte engineering (Table S1, ESI†),[11–13] designing polymer electrolytes (Tables S2 and S3, ESI†),[14–16] Li metal hosts fabrication,[17] and artificial solid–electrolyte interface (SEI) layer construction,[3,6] have already been explored. Among these approaches, varied polymer electrolytes, including solid polymer electrolytes (SPEs) and gel polymer electrolytes (GPEs), have aroused increasing interest due to their flexibility, leak-proofing, and excellent compatibility with the Li anode.[14–16] Specifically, polymer electrolytes with a high Li$^+$ transference number (t_{Li^+})[15] can alleviate Li dendrites growth and polymer electrolytes can suppress parasitic reactions between the Li anode and free solvent molecules.[18–21] Moreover, some polymer electrolytes with a fluorinated main chain can enhance the thermal stability of the electrolyte to reduce the thermal abuse hazards.[22] Thus, developing polymer electrolytes is imperative to simultaneously enhancing the cycle life and safety characteristics of LMBs.

Generally, there are two methods to fabricate polymer electrolytes: *ex situ* and *in situ* methods.[23,24] As for *ex situ* methods (SPE, such as casting,[25] electrospinning,[26] phase inversion/separation[27]), these polymer electrolytes have consistently underperformed in terms of ionic conductivity, interface compatibility, and processability.[23] Many efforts have been devoted to performing the *in situ* solidification of liquid electrolytes for preparing GPEs, to overcome these drawbacks.[24] Nevertheless, the extra nonelectrolytic monomers (such as acrylates/methacrylates,[24] 1,3-dioxolane[28,29]) and additional initiators are invariably highly chemically reactive and highly voltage vulnerable.[30] Differently, as the intrinsic material of an electrolyte, the Li salt anion is an ideal polymerization monomer. Previous reports suggest that Li salt anions can be fixed on a polymer chain to fabricate a conventional single-ion polymer electrolyte (SIPE), which is currently limited by its poor processability.[15] Hitherto, there are no methods to construct polymer electrolytes by polymerization of the Li salt anion. Taken together, we envision that an SIPE could be fabricated through a simple one-step *in situ* polymerization of Li salt anions, without any additional monomer or initiator.

Herein, we unprecedentedly explored an aluminum (Al)-based lithium salt (perfluoropinacolatoaluminate (LiFPA)) as a monomer precursor for constructing an SIPE (also belonging to GPE, abbreviated as 3D-SIPE-LiFPA) in LMBs by a thermal-induced one-step *in situ* polymerization. The as-constructed 3D-SIPE-LiFPA possessed exclusive characteristics compared with conventional GPEs and conventional SIPEs (Fig. 1a): (1) Al serves as the central atom of the 3D cross-linked polymerized

FPA$^-$ (poly-FPA) anion chain; (2) parts of the ethyl methyl carbonate (EMC) and fluoroethylene carbonate (FEC) molecules were fixed on the poly-FPA chain in a unique solvation structure. These unique structures could promote the formation of a protective and robust SEI layer enriched on LiF and Al-containing substances. Moreover, the as-constructed 3D-SIPE-LiFPA provided a high t_{Li^+} of 0.915 and high ionic conductivity of 2.48 mS cm^{-1} at 30 °C. It should be noted that the hitherto reported polymer electrolytes, constructed by either *ex situ* or *in situ* methods, could barely be used in practical LMBs (cathode ≥ 3.5 mA h cm^{-2}, Li ≤ 50 μm) (Tables S2 and S3, ESI†). Inspirationally, the electrochemical tests showed that 3D-SIPE-LiFPA enabled coin-type (80.8% after 236 cycles) and pouch-type (437 W h kg^{-1}, 95.4% after 60 cycles, injected electrolyte 2 g A h^{-1}) NCM811 (3.7 mA h cm^{-2})/Li (50 μm) LMBs to enjoy long cycle life. Encouragingly, accelerating rate calorimetry (ARC) measurements showed that 3D-SIPE-LiFPA enabled a significantly enhanced thermal safety characteristic of pouch-type 437 W h kg^{-1} NCM811/Li LMBs, delivering an increase in heat-releasing onset temperature (T_{onset}) and thermal runaway temperature (T_{tr}) by 34 °C and 72 °C, respectively. Our work will be an important milestone for polymer electrolytes, thus boosting the development of LMBs.

2. Results and discussion

2.1. Fabrication of 3D-SIPE-LiFPA

After heating at 60 °C for 12 h, the liquid-state 1 M LiFPA EMC/FEC electrolyte changed to gel state and its fluidity disappeared (Fig. 1b and Fig. S1, ESI†). The ^{1}H nuclear magnetic resonance (NMR) (Fig. 1c and Fig. S2a, ESI†) and ^{19}F NMR (Fig. 1d and Fig. S2b, ESI†) spectra showed that the peaks corresponding to EMC and FEC molecules remained unchanged during the gelation, suggesting that the EMC and FEC solvents did not participate in the polymerization process. From the ^{19}F NMR spectra (Fig. 1e and Fig. S2c, ESI†), the peak of FPA$^-$ disappeared after the gelation. These results indicate that the gelation originated from the polymerization of FPA$^-$ rather than the solvents. To further validate this conclusion, dry polymer powder obtained from 3D-SIPE-LiFPA was studied by X-ray diffraction (XRD, Fig. S3, ESI†), ^{19}F NMR (Fig. S4, ESI†), energy dispersive spectrometry (EDS) mapping (Fig. S5, ESI†), X-ray photoelectron spectroscopy (XPS) (Fig. S6, ESI†), and ToF-SIMS (Fig. 1f and g). Fig. S3 (ESI†) demonstrates that the dry polymer powder was amorphous, differentiated from the crystalline LiPFA powder. In the ^{19}F NMR spectra (Fig. S4, ESI†), the chemical shift of –CF$_3$ in the dry polymer powder and LiFPA was also different. The EDS-mapping results (Fig. S5 and Table S4, ESI†) revealed that C, O, F, and Al elements were homogenously distributed in the dry polymer powder. The existence of the species, *e.g.*, C–O, C–C, C–F, LiF, Al–O, *etc.*, could be corroborated by their characteristic XPS peaks (Fig. S6, ESI†). Additionally, as shown in the ToF-SIMS 3D element reconstruction (Fig. 1f) and corresponding depth profiles (Fig. 1g), Li$^+$, AlO$_2^+$, CF$_3^+$, and Li$_2$F$^+$ species were evenly distributed in the dry

2592 | *Energy Environ. Sci.*, 2023, **16**, 2591–2602

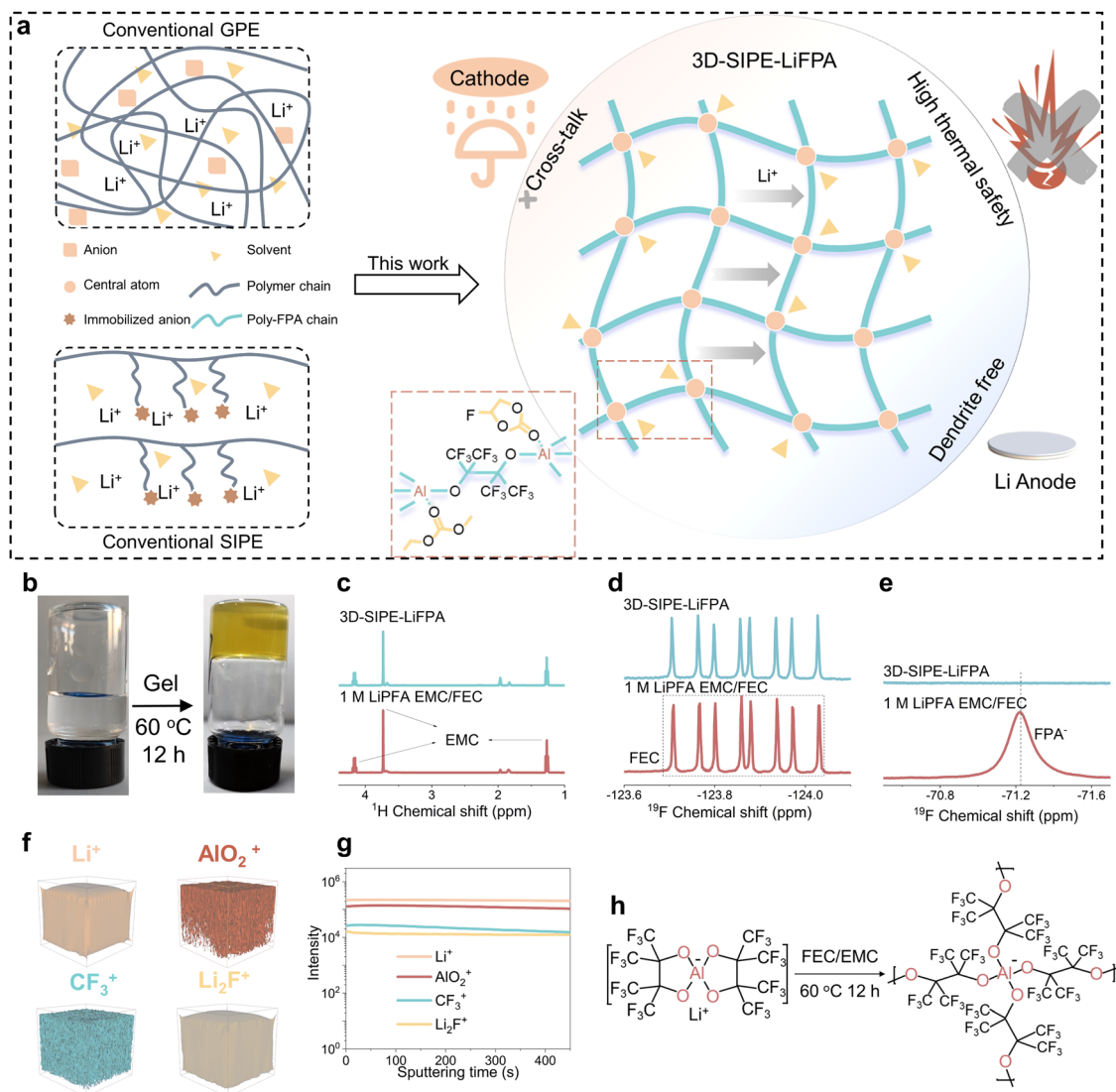This journal is © The Royal Society of Chemistry 2023

Fig. 1 Schematic illustration and characterizations of 3D-SIPE-LiFPA. (a) Conceptual sketch of a conventional GPE, conventional SIPE and as-constructed 3D-SIPE-LiFPA. (b) Optical images showing the liquid state electrolyte (1 M LiFPA EMC/FEC) and 3D-SIPE-LiFPA. (c) ^{1}H NMR, (d) ^{19}F NMR (−123.6 to −124.1 ppm), and (e) ^{19}F NMR (−70.5 to −71.7 ppm) spectra of 1 M LiFPA EMC/FEC and 3D-SIPE-LiFPA. ToF-SIMS, (f) 3D element reconstruction and (g) corresponding depth profiles of dry polymer powder obtained from 3D-SIPE-LiFPA. (h) Schematic illustration of the possible polymerization process of LiFPA.

polymer powder. Finally, the obtained dry polymer powder was dispersed in THF but could hardly be dissolved, suggesting its 3D cross-linked nature (Fig. S7, ESI†).[31,32] The possible polymerization process of LiFPA is illustrated in Fig. 1h. In summary, it was successfully confirmed that the gelation of the liquid-state electrolyte (1 M LiFPA EMC/FEC) could be ascribed to the 3D cross-linked polymerization of LiFPA, rather than the polymerization of EMC and FEC solvents.

2.2. Solvation structure of the as-constructed 3D-SIPE-LiFPA

The solvation structure of an electrolyte has great influence on electrode/electrolyte interfaces and Li dendrites growth.[33,34] To unveil the bulk structure of the as-constructed 3D-SIPE-LiFPA, Fourier transform infrared spectroscopy (FTIR), NMR, and diffusion ordered spectroscopy (DOSY) NMR characterizations were conducted. ^{7}Li NMR is sensitive to the coordinating

environment of Li^{+} in the solvation structure. Due to either a stronger solvent binding or stronger anion binding, the electron density around Li^{+} will increase, leading to an up-field shift (more negative) of ^{7}Li NMR.[35] In the ^{7}Li NMR results (Fig. 2a), the liquid electrolyte of 1 M LiFPA EMC/FEC displayed a more negative chemical shift (−0.875 ppm) than 1 M LiPF$_6$ EMC/FEC (−0.650 ppm), indicating a stronger interaction between the FPA[−] anion and Li^{+}. Moreover, the chemical shift decreased further from −0.875 ppm to −0.920 ppm after gelation, suggesting that the poly-FPA chain in 3D-SIPE-LiFPA possessed the strongest coordination ability with Li^{+}. This was indicative of increased contact ion pairs (Li^{+} and poly-FPA), which are ubiquitous in high (or locally high) salt concentration electrolytes and are favorable for forming protective solid–electrolyte interface (SEI) layers enriched with inorganic species.[4,5,33,36] Molecular dynamics (MD) simulation is always conducted to reveal the solvation structure of electrolytes.[34] Due to the

This journal is © The Royal Society of Chemistry 2023

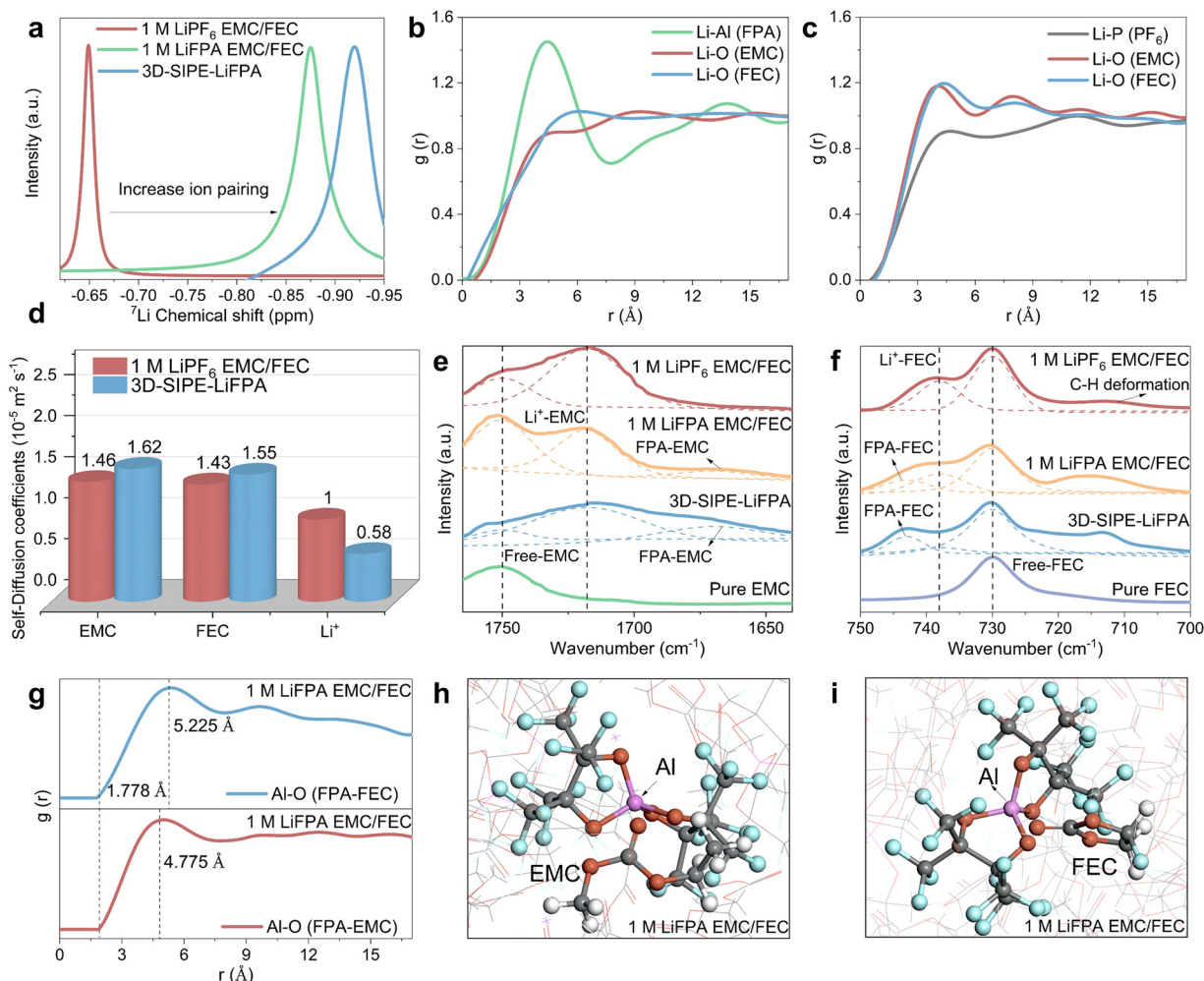*Energy Environ. Sci.*, 2023, **16**, 2591–2602 | **2593**

Fig. 2 Solvated structure of the as-constructed 3D-SIPE-LiFPA. (a) ^{7}Li NMR of 1 M LiPF$_6$ EMC/FEC, 1 M LiFPA EMC/FEC, and 3D-SIPE-LiFPA. RDF in MD simulations of the (b) 1 M LiFPA EMC/FEC and (c) 1 M LiPF$_6$ EMC/FEC. (d) Self-diffusion coefficients of EMC, FEC, and Li^{+} measured by ^{1}H, ^{19}F, and ^{7}Li DOSY NMR. FTIR spectra of (e) C=O stretching vibration of EMC and (f) C=O breathing vibration of FEC. (g) RDF of the 1 M LiFPA EMC/FEC. MD simulation snapshots of 1 M LiFPA EMC/FEC representing (h) FPA−EMC and (i) FPA−FEC.

large molecular weight of poly-FPA, the MD simulation for 3D-SIPE-LiFPA is quite difficult. Therefore, the MD simulations of 1 M LiFPA EMC/FEC and 1 M LiPF$_6$ EMC/FEC were conducted for comparison of the solvation structures. Fig. S8 (ESI†) presents snapshots of the solvation structure of 1 M LiFPA EMC/FEC and 1 M LiPF$_6$ EMC/FEC. From the radical distribution function (RDF), one can note that in the Li^{+} solvation shell of 1 M LiFPA EMC/FEC, the number of anions (FPA[−] *vs.* PF$_6$[−]) was increased and the amount of EMC/FEC was decreased compared with that for 1 M LiPF$_6$ EMC/FEC (Fig. 2b and c). These MD simulation results were well consistent with the ^{7}Li NMR results. The self-diffusion coefficients (obtained by DOSY NMR) of Li^{+} and solvent molecules had larger gaps in 3D-SIPE-LiFPA (*e.g.*, 1.04; 1.62 of EMC *vs.* 0.58 of Li^{+}) than 1 M LiPF$_6$ EMC/FEC (*e.g.*, 0.46; 1.46 of EMC *vs.* 1.0 of Li^{+}), suggesting the weaker coordination between the Li^{+} and solvents in 3D-SIPE-LiFPA (Fig. 2d), confirming the MD simulation results. The FTIR results provided further solvation structure information of these electrolytes. In Fig. 2e and f, the peaks located at 1750 and 730 cm^{−1} could be attributed to the C=O stretching vibration of free

EMC[37] and C=O breathing vibration of free FEC,[38] respectively. From 1 M LiPF$_6$ EMC/FEC, 1 M LiFPA EMC/FEC to 3D-SIPE-LiFPA, the coordination of Li^{+}–EMC (1718 cm^{−1}, Fig. 2e) and Li^{+}–FEC (738 cm^{−1}, Fig. 2f) gradually decreased, also demonstrating the weaker coordination between the Li^{+} and solvents in 3D-SIPE-LiFPA. Interestingly, apart from free EMC (1750 cm^{−1}), Li^{+}–EMC (1718 cm^{−1}), free FEC (730 cm^{−1}), and Li^{+}–FEC (738 cm^{−1}), the distinctive novel peaks centered at 1670 and 742 cm^{−1} could be ascribed to the coordination of EMC–FPA (EMC-Al) (Fig. 2e) and FEC–FPA (FEC-Al) (Fig. 2f), respectively. Moreover, after gelation, the EMC–FPA and FEC–FPA interactions become stronger. The MD simulations indicated that EMC/FEC solvent molecules had direct interaction with the Al of the FPA[−] anion (Fig. 2g–i). The EMC–FPA and FEC–FPA interactions were also illustrated by the Raman spectra (Fig. S9, ESI†). The density functional theory (DFT) simulations showed that LiFPA possessed the lowest LUMO energy compared with EMC, FEC, and LiPF$_6$ (Fig. S10a, ESI†), and the anion-solvent coordination (FPA–EMC, PFA–FEC) further decreased the LUMO energy of the FPA

2594 | *Energy Environ. Sci.*, 2023, **16**, 2591–2602

This journal is © The Royal Society of Chemistry 2023

anion (Fig. S10b, ESI†). In addition, due to having the lowest bond-breaking energy (−5.32 eV), FPA⁻ in the FPA–EMC coordination was more inclined to be reduced to form an SEI enriched with inorganic species (Fig. S11, ESI†). In summary, 3D-SIPE-LiFPA possessed a unique solvation structure, in which the Li⁺ solvation shell was enriched with poly-FPA anions and some EMC and FEC molecules were fixed on the poly-FPA chain. Given its high ionic conductivity (2.48 mS cm⁻¹, Fig. S12, ESI†), high t_{Li^+} (0.915, Fig. S13, ESI†), and excellent SEI forming ability, the as-constructed 3D-SIPE-LiFPA is a good potential candidate for Li anode protection.

2.3. Cycle life and thermal safety of NCM811/Li LMBs using 3D-SIPE-LiFPA

The as-constructed 3D-SIPE-LiFPA was evaluated in Li metal-based cells. First, Li/Cu and Li/Li cells using 3D-SIPE-LiFPA

demonstrated excellent Li plating/stripping behaviors (Fig. S14 and S15, ESI†). To validate its potential applications, the as-constructed 3D-SIPE-LiFPA was then evaluated in practical LMBs composed of a high areal capacity NCM811 cathode (3.7 mA h cm⁻², 210 mA h g⁻¹) and ultrathin (50 μm) Li anode. Encouragingly, when charged/discharged at 0.2C/0.3C rate for 236 cycles, NCM811/Li LMBs (2.8–4.3 V) using 3D-SIPE-LiFPA delivered a high-capacity retention of 80.8% (169.7 mA h g⁻¹/ 210.0 mA h g⁻¹) and a high average CE of 99.9% (Fig. 3a and Fig. S16a, ESI†). In contrast, NCM811/Li LMBs using 1 M LiPF₆ EMC/FEC (Fig. 3a and Fig. S16b, ESI†), 1 M LiPF₆ EC/EMC (Fig. S17a and b, ESI†), and 1 M LiFPA EMC/FEC (Fig. S17c and d, ESI†) suffered from sudden capacity failure within 80 cycles. Upon cycling, the NMC811/Li LMBs delivered a lower and more stable interfacial resistance when using 3D-SIPE-LiFPA (Fig. S18, ESI†). Moreover, due to the higher t_{Li^+} (0.915, Fig. S12, ESI†), lower
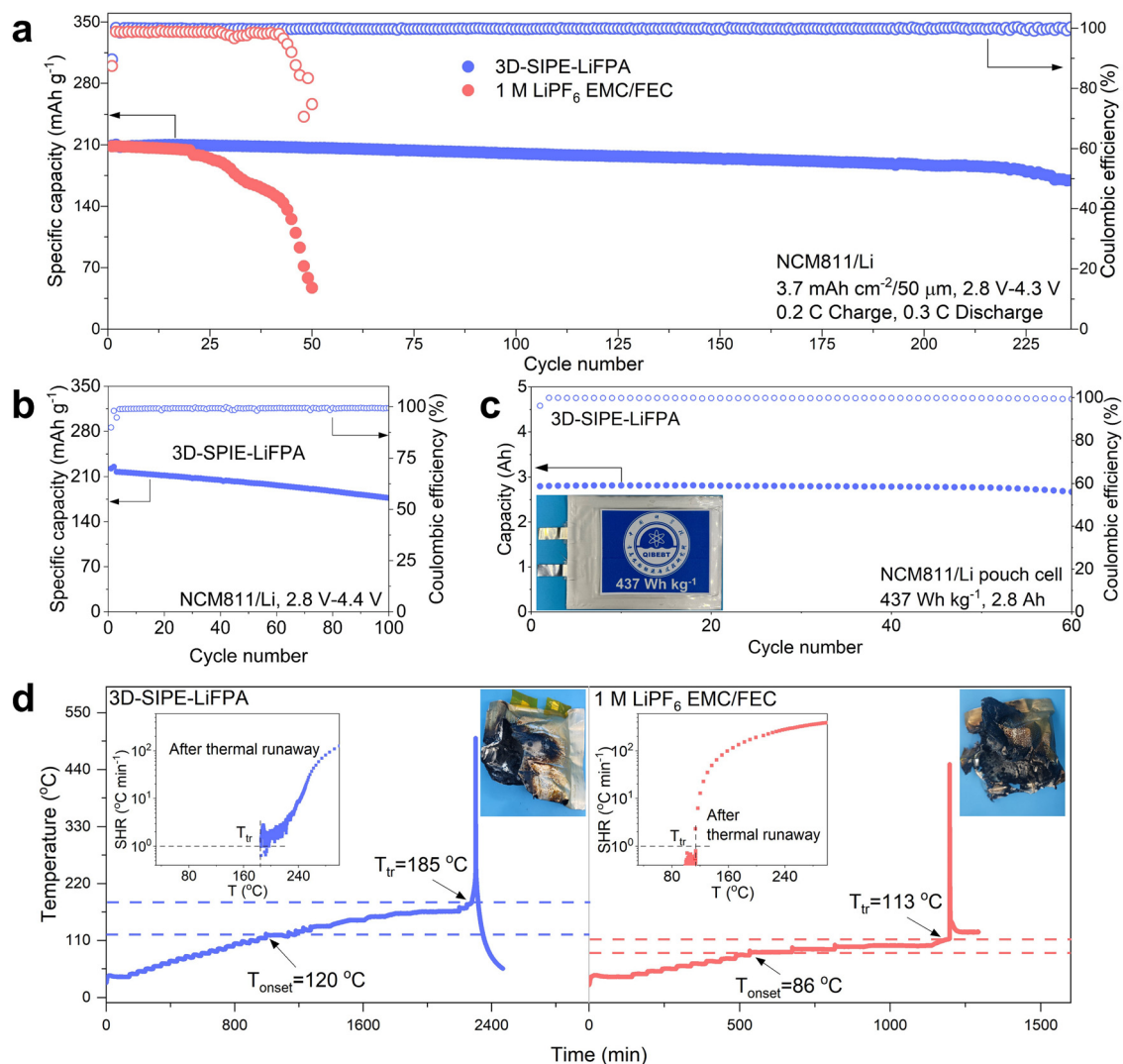

Fig. 3 Cycle life and thermal safety of NCM811/Li LMBs. (a) Cycling performances of NCM811/Li LMBs (2.8−4.3 V, 3.7 mA h cm⁻², 50 μm Li) using 3D-SIPE–LiFPA and 1 M LiPF₆ EMC/FEC. (b) Cycling performance of NCM811/Li LMBs (2.8−4.4 V, 3.7 mA h cm⁻², 50 μm Li) using 3D-SIPE–LiFPA. (c) Cycling performance of 2.8 A h (437 W h kg⁻¹) NCM811/Li pouch cells (2.8−4.3 V, 3.7 mA h cm⁻², 50 μm Li) using 3D-SIPE–LiFPA. (d) Thermal runaway features of 100% SOC NCM811/Li pouch cells in ARC tests.

This journal is © The Royal Society of Chemistry 2023

Energy Environ. Sci., 2023, **16**, 2591–2602 | **2595**

interfacial impedance (Fig. S18 and S19, ESI†), and the lower activation energy of Li$^+$ diffusion through the SEI layers (Fig. S20, ESI†), NCM811/Li LMBs using 3D-SIPE-LiFPA exhibited a slightly better rate capability than their counterpart (Fig. S21, ESI†). Fig. S22 (ESI†) shows that NCM811/Li LMBs using 3D-SIPE-LiFPA could also be operated under harsh temperature conditions, such as high temperatures (50 °C and 90 °C) and subzero temperatures (0 °C and −15 °C). The NCM811/Li LMBs using 3D-SIPE-LiFPA also demonstrated excellent moisture tolerance (Fig. S23, ESI†). Additionally, in the working voltage range of LMBs, 3D-SIPE-LiFPA possessed superior oxidative stability than its counterpart of 1 M LiPF$_6$ EMC/FEC (Fig. S24, ESI†). When the charge cut-off voltage was increased to 4.4 V, NCM811/Li LMBs using 3D-SIPE-LiFPA still showed high cycling stability (81.3% capacity retention after 100 cycles, 176.9 mA h g^{-1}/ 217.5 mA h g^{-1}; average CE of 99.5%) (Fig. 3b and Fig. S25, ESI†). The universality of the as-constructed 3D-SIPE-LiFPA was also verified by the long cycling stability of LiCoO$_2$/Li (3–4.45 V, 1.9 mA h cm^{-2}, 180 mA h g^{-1}; 3–4.6 V, 2.2 mA h cm^{-2}, 210 mA h g^{-1}) LMBs (Fig. S26, ESI†). More importantly, assembled pouch-type NCM811/Li prototype cells also presented excellent cycling stability (222 mA h, 300 W h kg^{-1}, 90.0% after 120 cycles; 2.8 A h, 437 W h kg^{-1}, 95.4% after 60 cycles) at a current density of 0.2C/0.3C rate (Fig. 3c and Fig. S27a–c, Table S6, ESI†). To the best of our knowledge, as-constructed 3D-SIPE-LiFPA could serve as the best polymer electrolyte for LMBs, considering the cycle life, areal capacity, safety, and energy density (Tables S2 and S3, ESI†).

Great efforts have been devoted to enhancing the cycle life of LMBs, but the thermal safety evaluation of LMBs with ultrahigh energy density is usually neglected.[39,40] Here, accelerating rate calorimetry (ARC, heat-wait-search (HWS) mode) was adopted to investigate the thermal features of pouch-type 2.8 A h NCM811/Li (3.7 mA h cm^{-2}, 50 μm Li) cells using the as-constructed 3D-SIPE-LiFPA (Fig. 3d and Fig. S28, ESI†). The heat-releasing onset temperature (T_{onset}) and thermal runaway temperature (T_{tr}) of a 100% SOC (state of charge) pouch cell using 3D-SIPE-LiFPA were 120 °C and 185 °C, respectively. In sharp contrast, the T_{onset} and T_{tr} of the control cell using 1 M LiPF$_6$ EMC/FEC were 86 °C and 113 °C, respectively. Also, the interval times between T_{onset} and T_{tr} were 1268 min and 652 min for 3D-SIPE-LiFPA and 1 M LiPF$_6$ EMC/FEC, respectively. In addition, the self-heating rate (SHR) after thermal runway increased more slowly when using 3D-SIPE-LiFPA (insets in Fig. 3d and Fig. S28, ESI†). The pouch cells using two electrolytes were both severely damaged after thermal runaway (insets in Fig. 3d). Nevertheless, improving the critical temperatures (T_{onset} and T_{tr}) and prolonging the self-heating time by 3D-SIPE-LiFPA could reduce potential damage when LMBs experience thermal runaway. Subsequently, differential scanning calorimetry (DSC) (Fig. S29, ESI†) and ARC (Fig. S30 and S31, ESI†) experiments were conducted to uncover the underpinning mechanisms of 3D-SIPE-LiFPA in improving the safety of LMBs. The significantly enhanced safety characteristics of 100% SOC NCM811/Li pouch cells mainly originated from the greatly alleviated Li anode heat released by 3D-SIPE-LiFPA. All these encouraging results underlie

the superiority of using the *in situ*-polymerized FPA$^-$ anion for obtaining long cycle life and high thermal safety LMBs. Furthermore, the ARC data of LMBs with different electrolytes in previous reports are summarized in Table S7 (ESI†) for reference.

2.4. Synchrotron X-ray computed tomography of NCM811/Li LMBs using 3D-SIPE-LiFPA

In situ SXCT was employed to reveal the crucial role of 3D-SIPE-LiFPA in enabling the superior cycling performance of NCM811/Li LMBs. A digital photograph and corresponding illustration of the customized electrochemical tomography cell (tomo-cell) are shown in Fig. S32a (ESI†), along with a schematic demonstration of the employed synchrotron X-ray imaging beamline in Fig. S32b (ESI†).[41–43] It was noteworthy that the reconstructed grayscale SXCT images possessing distinct contrasts were correlated with the different X-ray absorbing capabilities of the constituent atoms in the measured samples. Specifically, the bright and dark region corresponded to high-z atom-containing components (*e.g.*, NCM811) and low-z atom-containing components (*e.g.*, Li and separator), respectively.[44,45] The uncycled state of NCM811/Li tomo-cell is given in Fig. S33 (ESI†), from which different cell components, such as the NCM811 cathode, glass fiber separator (GF-A), and Li anode are clearly discernable. At the fully charged state in the first cycle, the electrochemically deposited metallic Li layer was much thinner and denser in the NCM811/Li tomo-cell using 3D-SIPE-LiFPA (Fig. S34a$_1$–a$_3$, ESI†) compared with that using 1 M LiPF$_6$ EMC/FEC (Fig. S34b$_1$–b$_3$, ESI†).

On the basis of the different X-ray absorbing capabilities of each component, internal views of NCM811/Li tomo-cells using either 3D-SIPE-LiFPA or the control 1 M LiPF$_6$ EMC/FEC after 10 cycles in the fully discharged state (Fig. 4a$_1$ and b$_1$) are shown in Fig. 4a$_2$ and b$_2$. The gray values of each component along with the white specific dashed lines in Fig. 4a$_2$ and b$_2$ are shown in Fig. 4a$_3$ and b$_3$, respectively. A closer look at the Li/separator interface was obtained from the enlarged area (Fig. 4a$_4$, 2D cross-section) of the red rectangle in Fig. 4a$_2$. Also, 3D volume renderings of the cropped yellow rectangle region (in Fig. 4a$_4$) are illustrated in Fig. 4a$_5$ (horizontal view) and Fig. 4a$_6$ (3D view), revealing a thin and homogeneous corrosion layer (a mixture of SEI, dead Li, other byproducts, and voids/cracks, *etc.*). In sharp contrast, a thick and heterogeneous corrosion layer was observed in the control cell (Fig. 4b$_2$ and b$_4$–b$_6$).[46,47] As shown in Fig. 4a$_7$ (2D cross-section) and Fig. 4a$_8$ (3D volume rendering), the NCM811 electrode maintained a high integrity without cracking when using 3D-SIPE-LiFPA. However, severe electrode cracking was observed in the control cell (Fig. 4b$_7$, 2D cross-section; Fig. 4b$_8$, 3D volume rendering). These great differences are believed to be associated with the electrode/electrolyte interface properties, which will be deeply discussed in the following sections. With a further look at the Li anode side in the 10-times cycled tomo-cell using 1 M LiPF$_6$ EMC/FEC in Fig. 4b$_2$, one can notice some unusual red regions appearing within the corrosion layer. By analyzing the gray values of these red regions as shown in Fig. 4b$_3$, one can note the same extent of X-ray absorbing capability of these red regions to that of the NCM811 cathode.

2596 | *Energy Environ. Sci.*, 2023, **16**, 2591–2602

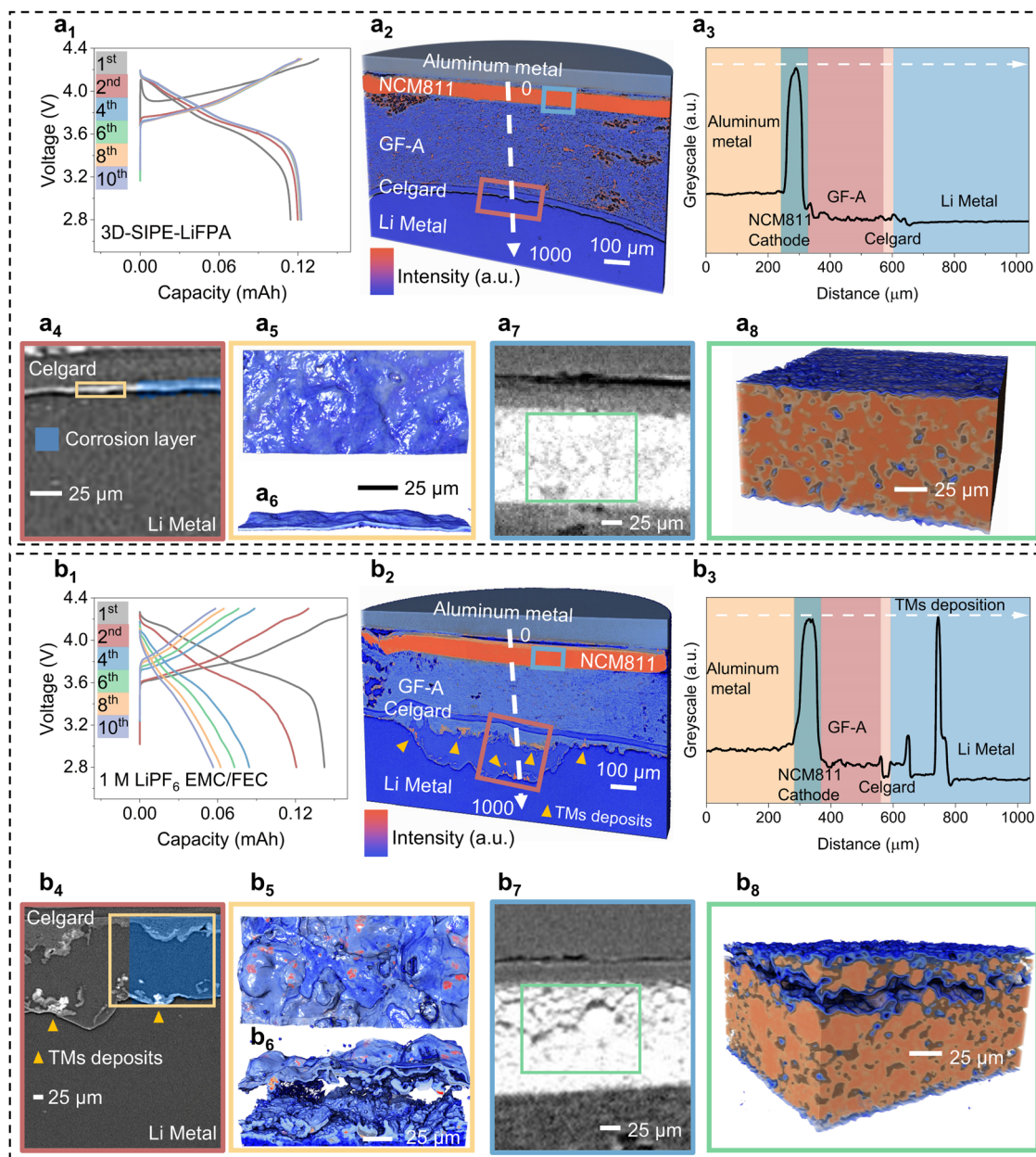This journal is © The Royal Society of Chemistry 2023

Fig. 4 Synchrotron X-ray tomography of NCM811/Li LMBs. Representative charge–discharge curves of the 10-times cycled tomo-cells of NCM811/Li using 3D-SIPE-LiFPA (a_1) and 1 M LiPF$_6$ EMC/FEC (b_1). (a_2 and b_2) 3D volume renderings of the reconstructed X-ray tomography datasets. (a_3 and b_3) Line profiles of the X-ray absorption intensity along the white dashed arrow lines in (a_2) and (b_2), respectively. Cross-sections of tomo-cells at the Li anode side (a_4 and b_4) and cathode side (a_7 and b_7). (a_5, a_6 and b_5, b_6) 3D volume renderings of the cropped yellow rectangle region in (a_4) and (b_4), respectively. (a_8 and b_8) 3D rendering images of the enlarged view of the green rectangle region in (a_7) and (b_7), respectively.

These results confirmed the dissolution–migration–deposition of TMs from the NCM811 cathode to Li anode when using 1 M LiPF$_6$ EMC/FEC. Moreover, the 2D cross-section (Fig. 4b$_4$) and 3D volume renderings (Fig. 4b$_5$ and b$_6$) demonstrated that large amounts TMs were distributed within the corrosion layer (white regions in Fig. 4b$_4$ and red regions in Fig. 4b$_5$ and b$_6$). The situation was even more severe at the 50th cycle (Fig. S35b$_2$ and b$_3$, ESI†). In contrast, no such scenario was observed when using 3D-SIPE-LiFPA (Fig. 4a$_2$, a$_4$–a$_6$ and Fig. S35a$_2$, a$_3$, ESI†). The inhibited TMs dissolution was further verified by ToF-SIMS (Fig.

S36, ESI†), XPS (Fig. S37, ESI†), and ICP-MS (Fig. S38, ESI†). In summary, inhibiting TMs dissolution from the NCM811 cathode and blocking TMs deposition on the Li metal anode may contribute to homogeneous Li plating/stripping, ensuring the long cycle life of NCM811/Li LMBs.

2.5. Characterization of the cycled Li anode

Further characterizations, such as ToF-SIMS and on-line deuterium-oxide (D$_2$O) titration, were conducted to decipher the crucial role of 3D-SIPE-LiFPA in protecting the Li anode,

This journal is © The Royal Society of Chemistry 2023

Energy Environ. Sci., 2023, **16**, 2591–2602 | **2597**

which was disassembled from NMC811/Li (3.7 mA h cm^{-2}, 50 μm) LMBs after 50 cycles. From the top-view SEM image, it could be seen that the Li anode surface was more compact and smoother when using 3D-SIPE-LiFPA compared with 1 M LiPF$_6$ EMC/FEC (Fig. S39, ESI†). The cross-section SEM of the Li anode cycled in 3D-SIPE-LiFPA showed negligible thickness change (53 μm), while that cycled in 1 M LiPF$_6$ EMC/FEC displayed a pulverized feature with a maximum thickness of 73 μm (Fig. 5a–c). To uncover the origins behind these differences, the SEI components of the cycled Li anodes were identified. By comparing the ToF-SIMS 3D element reconstruction of Li anodes cycled in both electrolytes (Fig. 5d and Fig. S40, ESI†), one can note that the SEI layer derived from 3D-SIPE-LiFPA was enriched in inorganic Al-containing species (Al$^+$ and AlF$_4^-$, through the SEI) and LiF (Li$_2$F$^+$, through the SEI), and some organic C–F species (CF$_3^-$ and C$_3$F$_5$O$^-$, outer layer of SEI). Moreover, from the depth-profiling XPS spectra,

the formation of other organic species (such as C–C, C–H, C–O) in the SEI of the Li anode was suppressed when cycled in 3D-SIPE-LiFPA (Fig. S41 and S42, ESI†). These results were in accordance with the calculation results that poly-FPA was more inclined to decompose to generate an inorganic-species-enriched SEI layer, which could inhibit the decomposition of the solvents. In addition, the formed unique SEI layer provides extra benefits besides protecting the Li anode: (1) the out layer enriched in C–F species can act as effective Lewis bases to absorb Li$^+$, lowering the local fluctuation of Li$^+$;[48] (2) Al-containing species and LiF with a high interfacial energy and low Li$^+$ diffusion barrier can facilitate reversible Li$^+$ stripping/plating without dendrites growth. In previous reports,[49–51] it was suggested that the accumulation of LiH contributes to Li anode failure. Here, on-line D$_2$O titration gas analysis mass spectrometry (MS) was employed to quantify LiH (Fig. 5e).[52] When cycled in 1 M LiPF$_6$ EMC/FEC, the D$_2$/HD ratio was 8.66,
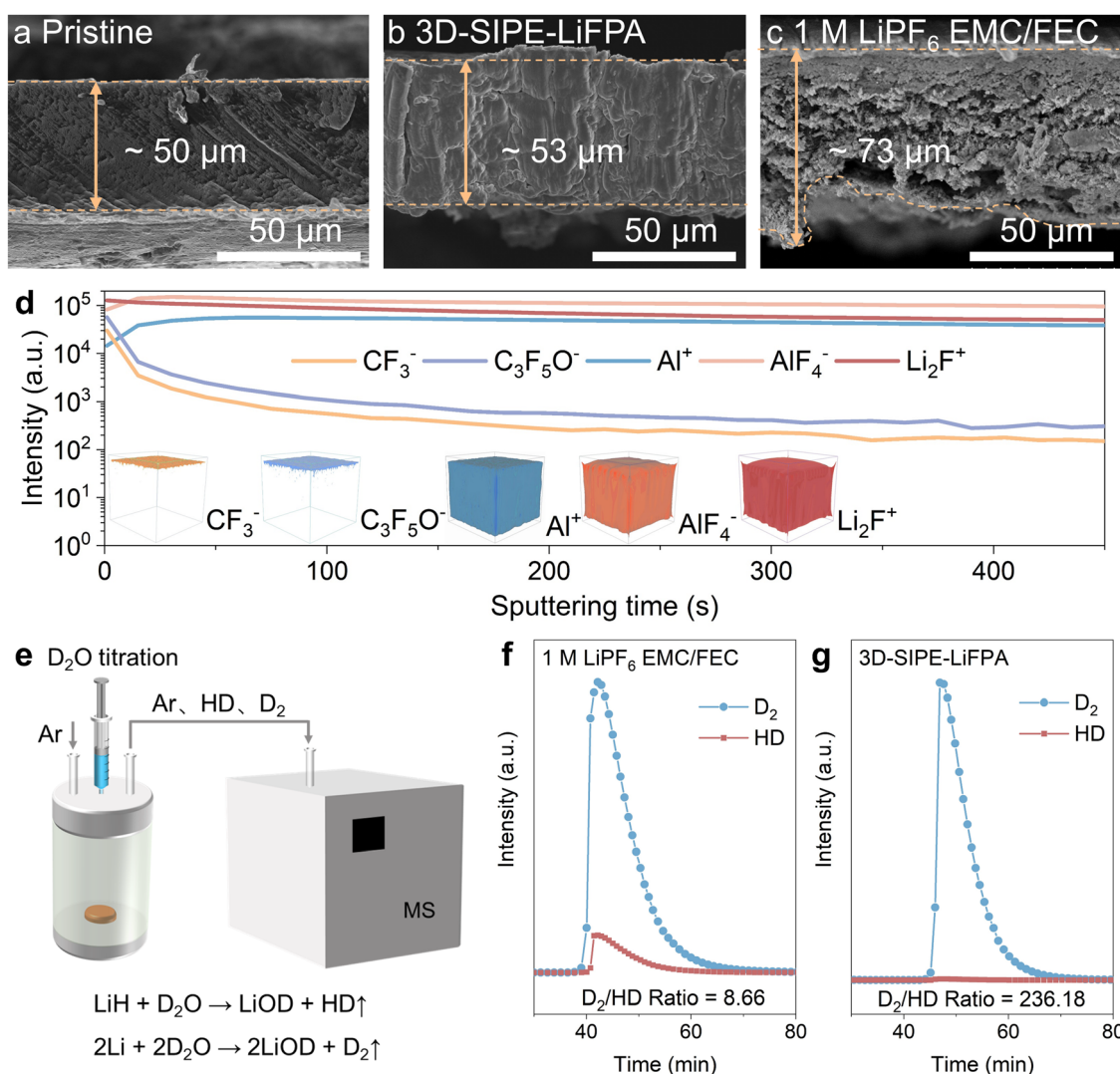

Fig. 5 Characterizations of the cycled Li anode. (a–c) Typical cross-section SEM of (a) pristine Li anode and that cycled in (b) 3D-SIPE-LiFPA and (c) 1 M LiPF$_6$ EMC/FEC. (d) ToF-SIMS 3D reconstruction and corresponding depth profiles of Li anode cycled in 3D-SIPE-LiFPA. (e) Schematic illustration of the on-line D$_2$O titration gas analysis MS system. The D$_2$ and HD evolution rate curves after D$_2$O titration on the Li anode cycled in (f) 1 M LiPF$_6$ EMC/FEC and (g) 3D-SIPE-LiFPA. The Li anode was disassembled from NMC811/Li (3.7 mA h cm^{-2}, 50 μm) LMBs after 50 cycles.

2598 | *Energy Environ. Sci.*, 2023, **16**, 2591–2602

This journal is © The Royal Society of Chemistry 2023

suggesting that large amounts of LiH were formed in the cycled Li anode (Fig. 5f). Encouragingly, the formation of LiH was greatly suppressed (D_2/HD ratio was 236.18) when using 3D-SIPE-LiFPA (Fig. 5g). Additionally, the lower generation of CO_2 and CH_3D indicated the inhibited solvents decomposition on the Li anode (Fig. S43, ESI†).[52] In summary, the suppressed TMs deposition, inhibited electrolyte decomposition, alleviated LiH formation, together with the unique SEI layer and high t_{Li^+} collectively contributed to protecting the Li anode from rapid failure when using 3D-SIPE-LiFPA.

2.6. In-depth analysis of the cathode/electrolyte interface

It is also necessary to unveil the important role of 3D-SIPE-LiFPA in stabilizing the NCM811 cathode. There were less micro-cracks and micro-pores with the NCM811 particles when cycled in 3D-SIPE-LiFPA (Fig. S44a–c, ESI†). Then, depth-profiling XPS and ToF-SIMS were conducted to disclose the components of the CEI layer. For 3D-SIPE-LiFPA and 1 M $LiPF_6$ EMC/FEC, an M–O bond signal from the O 1s XPS spectra appeared after 60 s and 120 s etching, respectively (Fig. S45a and c, ESI†). This confirmed that 3D-SIPE-LiFPA favored the formation of a much thinner CEI layer, consistent with the high-resolution transmission electron microscopy (HRTEM) images (Fig. 6a, b and Fig. S46, ESI†). The HRTEM images also indicated that the surface crystal structure of the NCM811 cathode was better preserved when cycled in 3D-SIPE-LiFPA (Fig. 6a, b and Fig. S46 (ESI†), Fast Fourier transform). Additionally, there were many high-valence-Al-containing species (AlF$_3$ 76.2 eV, AlF$_4$ 75.3 eV, Al_2O_3 74.5 eV; Al 2p, Fig. 6c)
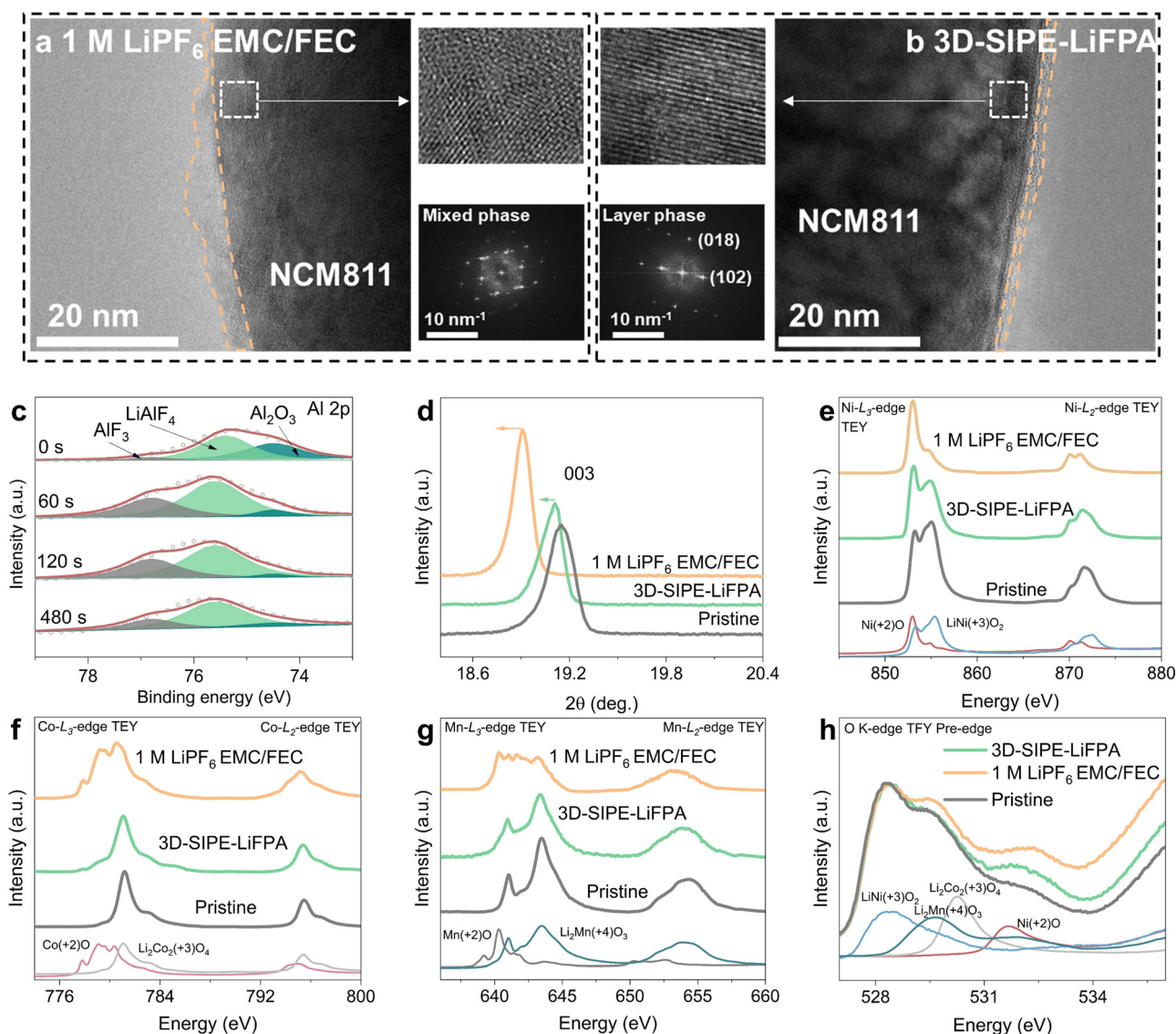

Fig. 6 Characterizations of the cycled NCM811 cathodes. HRTEM analyses of the cycled NCM811 after 50 cycles using different electrolytes: (a) 1 M $LiPF_6$ EMC/FEC, (b) 3D-SIPE-LiFPA. (c) Al 2p XPS spectra of the NCM811 cathode. (d) XRD of NCM811 before and after 50 cycles. (e–g) Ni, Co, Mn $L_{2,3}$-edge XAS spectra in the TEY mode and (h) O K-edge XAS spectra in the TFY mode of the measured NCM811 cathodes: pristine (black line), cycled in 3D-SIPE-LiFPA (green line), and cycled in 1 M $LiPF_6$ EMC/FEC electrolyte (yellow line). The measured NCM811 cathodes were harvested from NCM811/Li LMBs (50 μm, 3.7 mA h cm^{-2}, 2.8–4.3 V) after 50 cycles.

This journal is © The Royal Society of Chemistry 2023

Energy Environ. Sci., 2023, **16**, 2591–2602 | **2599**

and LiF (684.8 eV, F1s, Fig. S45b, ESI†), some of which were also identified by ToF-SIMS (Fig. S47, ESI†). These high-valence-Al-containing species derived from 3D-SIPE-LiFPA could be expected to improve the stability of the CEI layer and bulk structure of NCM811.[7] In contrast, the large formation amounts of LiF, P–O, and P–F species (Fig. S45c, d and S48, ESI†) in the CEI layer indicated the severe decomposition of 1 M $LiPF_6$ EMC/FEC.[7,53] The XRD pattern also revealed that the bulk crystal structure of NCM811 cathode was better preserved when cycled in 3D-SIPE-LiFPA (Fig. 6d and Fig. S49, ESI†), confirming the protective effect of the as-formed CEI layer.

The electronic structures of Ni, Co, and Mn ions in the NCM811 cathode were studied by measuring soft XAS at the $L_{2,3}$-edge of 3d elements. XAS is a powerful tool to determine the valence states,[54–56] local bonding environment,[57,58] and spin state[59,60] of the studied system. Fig. 6e shows the Ni-$L_{2,3}$ XAS spectra measured by the total electron yield (TEY) mode (surface sensitive, with a probing depth of approximately 4 nm) for the pristine NCM811, and NCM811 cycled in 3D-SIPE-LiFPA and 1 M $LiPF_6$ EMC/FEC. The XAS of NiO and $LiNiO_2$ served as references of Ni^{2+} and Ni^{3+}, respectively. When cycled in 3D-SIPE-LiFPA, the decrease in the oxidation state of Ni ions from Ni^{3+} to Ni^{2+} was significantly suppressed. Similarly, the transition of Co^{3+} to Co^{2+} (Fig. 6f), as well as the transition of Mn^{4+} to Mn^{3+} and Mn^{2+} (Fig. 6g) were also obviously inhibited when using 3D-SIPE-LiFPA.[61–63] The O K-edge XAS spectra in the total fluorescence yield mode (TFY, bulk-structure sensitive, several microns beneath the sample surface)[64–67] showed a lower Ni^{2+} content when using 3D-SIPE-LiFPA (Fig. 6h), in line with the Ni-$L_{2,3}$ XAS result. It is noted here that low valence TMs will be easily dissolved into the electrolytes.[68] Thus, when using 3D-SIPE-LiFPA, a thin and homogeneous CEI layer inhibits the decrease in the oxidation state of TMs, eventually suppressing its dissolution from the NCM811 cathode.

3. Conclusions

In this work, a single-ion conductive polymer electrolyte 3D-SIPE-LiFPA was successfully fabricated by the thermal-induced *in situ* polymerization of LiFPA. The Li^+ solvation shell of 3D-SIPE-LiFPA was enriched in poly-FPA, upon which were fixed some EMC and FEC molecules. The as-constructed 3D-SIPE-LiFPA endowed practical NCM811/Li LMBs with both excellent cycle life and high safety. Specifically, the successful protection of the Li anode by 3D-SIPE-LiFPA was ascribed to the suppressed TMs deposition, inhibited electrolyte decomposition, and alleviated LiH generation, together with the formation of a unique SEI layer enriched in inorganic Al-containing species. As for the NCM811 cathode, the 3D-SIPE-LiFPA-derived CEI layer prevented the decrease in the TM ions valence state and in turn blocked TMs dissolution and the crystal structure destruction. Our work sets a precedent of a strategy for polymerizing lithium salt as a polymer electrolyte, which simultaneously enables obtaining practical LMBs with excellent cycle life and high thermal safety.

Author contributions

S. Z. was the first author of this work. G. C., Z. C., and G. X. conceived the idea for the project. S. Z., Z. C. and G. X. designed the electrochemical experiments. S. Z., L. L., and B. X. performed the electrochemical experiments. P. H. provided the cathode materials. X. D. and S. Z. conducted the theoretical calculations. J. L. and S. D. conducted on-line D_2O titration experiments. X. Z. and L. H. performed the ARC experiments and processed the corresponding data. F. S., A. H., I. M. and S. Z. performed the SXCT measurement. J. M., Z. H., A. C. K., H. J. L., C. Y. K., and C. T. C. contributed to the XAS measurement. G. X., Z. C. and S. Z. wrote the manuscript with the help from all co-authors, and all authors contributed to interpretation of the data.

Conflicts of interest

There are no conflicts to declare.

Acknowledgements

References

1 Z. Yu, Y. Cui and Z. Bao, *Cell Rep. Phys. Sci.*, 2020, **1**, 100119.
2 G. Zhou, L. Xu, G. Hu, L. Mai and Y. Cui, *Chem. Rev.*, 2019, **119**, 11042–11109.
3 M. D. Tikekar, S. Choudhury, Z. Tu and L. A. Archer, *Nat. Energy*, 2016, **1**, 1–7.
4 Z. Yu, P. E. Rudnicki, Z. Zhang, Z. Huang, H. Celik, S. T. Oyakhire, Y. Chen, X. Kong, S. C. Kim, X. Xiao, H. Wang, Y. Zheng, G. A. Kamat, M. S. Kim, S. F. Bent, J. Qin, Y. Cui and Z. Bao, *Nat. Energy*, 2022, **7**, 94–106.
5 Z. Yu, H. Wang, X. Kong, W. Huang, Y. Tsao, D. G. Mackanic, K. Wang, X. Wang, W. Huang, S. Choudhury, Y. Zheng, C. V. Amanchukwu, S. T. Hung,

2600 | *Energy Environ. Sci.*, 2023, **16**, 2591–2602

This journal is © The Royal Society of Chemistry 2023

Y. Ma, E. G. Lomeli, J. Qin, Y. Cui and Z. Bao, *Nat. Energy*, 2020, **5**, 526–533.

6 Z. Yu, D. G. Mackanic, W. Michaels, M. Lee, A. Pei, D. Feng, Q. Zhang, Y. Tsao, C. V. Amanchukwu, X. Yan, H. Wang, S. Chen, K. Liu, J. Kang, J. Qin, Y. Cui and Z. Bao, *Joule*, 2019, **3**, 2761–2776.

7 L. Li, G. Xu, S. Zhang, S. Dong, S. Wang, Z. Cui, X. Du, C. Wang, B. Xie, J. Du, X. Zhou and G. Cui, *ACS Energy Lett.*, 2022, **7**, 591–598.

8 C. Jin, T. Liu, O. Sheng, M. Li, T. Liu, Y. Yuan, J. Nai, Z. Ju, W. Zhang, Y. Liu, Y. Wang, Z. Lin, J. Lu and X. Tao, *Nat. Energy*, 2021, **6**, 378–387.

9 F. Liu, R. Xu, Y. Wu, D. T. Boyle, A. Yang, J. Xu, Y. Zhu, Y. Ye, Z. Yu, Z. Zhang, X. Xiao, W. Huang, H. Wang, H. Chen and Y. Cui, *Nature*, 2021, **600**, 659–663.

10 W. Li, U. H. Kim, A. Dolocan, Y. K. Sun and A. Manthiram, *ACS Nano*, 2017, **11**, 5853–5863.

11 G. Xu, X. Shangguan, S. Dong, X. Zhou and G. Cui, *Angew. Chem., Int. Ed.*, 2020, **59**, 3400–3415.

12 J. G. Zhang, W. Xu, J. Xiao, X. Cao and J. Liu, *Chem. Rev.*, 2020, **120**, 13312–13348.

13 H. Wang, Z. Yu, X. Kong, S. C. Kim, D. T. Boyle, J. Qin, Z. Bao and Y. Cui, *Joule*, 2022, **6**, 588–616.

14 M. J. Lee, J. Han, K. Lee, Y. J. Lee, B. G. Kim, K. N. Jung, B. J. Kim and S. W. Lee, *Nature*, 2022, **601**, 217–222.

15 J. Zhu, Z. Zhang, S. Zhao, A. S. Westover, I. Belharouak and P. F. Cao, *Adv. Energy Mater.*, 2021, **11**, 2003836.

16 P. Ding, Z. Lin, X. Guo, L. Wu, Y. Wang, H. Guo, L. Li and H. Yu, *Mater. Today*, 2021, **51**, 449–474.

17 C. Niu, H. Pan, W. Xu, J. Xiao, J. G. Zhang, L. Luo, C. Wang, D. Mei, J. Meng, X. Wang, Z. Liu, L. Mai and J. Liu, *Nat. Nanotechnol.*, 2019, **14**, 594–601.

18 K. Deng, Q. Zeng, D. Wang, Z. Liu, Z. Qiu, Y. Zhang, M. Xiao and Y. Meng, *J. Mater. Chem. A*, 2020, **8**, 1557–1577.

19 D. M. Reinoso and M. A. Frechero, *Energy Storage Mater.*, 2022, **52**, 430–464.

20 C. Zhang, T. Jin, G. Cheng, S. Yuan, Z. Sun, N. W. Li, L. Yu and S. Ding, *J. Mater. Chem. A*, 2021, **9**, 13388–13401.

21 H. Zhang, Y. Chen, C. Li and M. Armand, *SusMat*, 2021, **1**, 24–37.

22 S. J. Yang, N. Yao, F. N. Jiang, J. Xie, S. Y. Sun, X. Chen, H. Yuan, X. B. Cheng, J. Q. Huang and Q. Zhang, *Angew. Chem., Int. Ed.*, 2022, **61**, e202214545.

23 Y. Zhao, Y. Bai, W. Li, M. An, Y. Bai and G. Chen, *Chem. Mater.*, 2020, **32**, 6811–6830.

24 V. Vijayakumar, B. Anothumakkool, S. Kurungot, M. Winter and J. R. Nair, *Energy Environ. Sci.*, 2021, **14**, 2708–2788.

25 X. Zhang, T. Liu, S. Zhang, X. Huang, B. Xu, Y. Lin, B. Xu, L. Li, C. W. Nan and Y. Shen, *J. Am. Chem. Soc.*, 2017, **139**, 13779–13785.

26 S. N. Banitaba, D. Semnani, E. Heydari-Soureshjani, B. Rezaei and A. A. Ensafi, *Solid State Ionics*, 2020, **347**, 115252.

27 Y. Chen, Y. Shi, Y. Liang, H. Dong, F. Hao, A. Wang, Y. Zhu, X. Cui and Y. Yao, *ACS Appl. Energy Mater.*, 2019, **2**, 1608–1615.

28 Q. Zhao, X. Liu, S. Stalin, K. Khan and L. A. Archer, *Nat. Energy*, 2019, **4**, 365–373.

29 C. Z. Zhao, Q. Zhao, X. Liu, J. Zheng, S. Stalin, Q. Zhang and L. A. Archer, *Adv. Mater.*, 2020, **32**, 1905629.

30 Z. Lv, Q. Zhou, S. Zhang, S. Dong, Q. Wang, L. Huang, K. Chen and G. Cui, *Energy Storage Mater.*, 2021, **37**, 215–223.

31 W. Fan, N. W. Li, X. Zhang, S. Zhao, R. Cao, Y. Yin, Y. Xing, J. Wang, Y. G. Guo and C. Li, *Adv. Sci.*, 2018, **5**, 1800559.

32 J. C. de Haro, E. Tatsi, L. Fagiolari, M. Bonomo, C. Barolo, S. Turri, F. Bella and G. Griffini, *ACS Sustainable Chem. Eng.*, 2021, **9**, 8550–8560.

33 S. Liu, X. Ji, N. Piao, J. Chen, N. Eidson, J. Xu, P. Wang, L. Chen, J. Zhang, T. Deng, S. Hou, T. Jin, H. Wan, J. Li, J. Tu and C. Wang, *Angew. Chem., Int. Ed.*, 2021, **60**, 3661–3671.

34 J. Holoubek, H. Liu, Z. Wu, Y. Yin, X. Xing, G. Cai, S. Yu, H. Zhou, T. A. Pascal, Z. Chen and P. Liu, *Nat. Energy*, 2021, **6**, 303–313.

35 Y. Chen, Z. Yu, P. Rudnicki, H. Gong, Z. Huang, S. C. Kim, J. C. Lai, X. Kong, J. Qin, Y. Cui and Z. Bao, *J. Am. Chem. Soc.*, 2021, **143**, 18703–18713.

36 Z. Zhang, Y. Li, R. Xu, W. Zhou, Y. Li, S. T. Oyakhire, Y. Wu, J. Xu, H. Wang, Z. Yu, D. T. Boyle, W. Huang, Y. Ye, H. Chen, J. Wan, Z. Bao, W. Chiu and Y. Cui, *Science*, 2022, **375**, 66–70.

37 Y. Zou, Z. Cao, J. Zhang, W. Wahyudi, Y. Wu, G. Liu, Q. Li, H. Cheng, D. Zhang, G. T. Park, L. Cavallo, T. D. Anthopoulos, L. Wang, Y. K. Sun and J. Ming, *Adv. Mater.*, 2021, **33**, 2102964.

38 T. Hou, G. Yang, N. N. Rajput, J. Self, S. W. Park, J. Nanda and K. A. Persson, *Nano Energy*, 2019, **64**, 103881.

39 L. Huang, T. Lu, G. Xu, X. Zhang, Z. Jiang, Z. Zhang, Y. Wang, P. Han, G. Cui and L. Chen, *Joule*, 2022, **6**, 906–922.

40 R. Chen, A. M. Nolan, J. Lu, J. Wang, X. Yu, Y. Mo, L. Chen, X. Huang and H. Li, *Joule*, 2020, **4**, 812–821.

41 F. Sun, D. Zhou, X. He, M. Osenberg, K. Dong, L. Chen, S. Mei, A. Hilger, H. Markötter, Y. Lu, S. Dong, S. Marathe, C. Rau, X. Hou, J. Li, M. C. Stan, M. Winter, R. Dominko and I. Manke, *ACS Energy Lett.*, 2019, **5**, 152–161.

42 F. Sun, X. He, X. Jiang, M. Osenberg, J. Li, D. Zhou, K. Dong, A. Hilger, X. Zhu, R. Gao, X. Liu, K. Huang, D. Ning, H. Markötter, L. Zhang, F. Wilde, Y. Cao, M. Winter and I. Manke, *Mater. Today*, 2019, **27**, 21–32.

43 F. Sun, C. Yang, I. Manke, L. Chen and S. Dong, *Mater. Today*, 2020, **38**, 7–9.

44 F. Tang, Z. Wu, C. Yang, M. Osenberg, A. Hilger, K. Dong, H. Markotter, I. Manke, F. Sun, L. Chen and G. Cui, *Small Methods*, 2021, **5**, 2100557.

45 F. Sun, C. Wang, M. Osenberg, K. Dong, S. Zhang, C. Yang, Y. Wang, A. Hilger, J. Zhang, S. Dong, H. Markötter, I. Manke and G. Cui, *Adv. Energy Mater.*, 2022, **12**, 2103714.

46 F. Sun, L. Zielke, H. Markotter, A. Hilger, D. Zhou, R. Moroni, R. Zengerle, S. Thiele, J. Banhart and I. Manke, *ACS Nano*, 2016, **10**, 7990–7997.

47 F. Sun, M. Osenberg, K. Dong, D. Zhou, A. Hilger, C. J. Jafta, S. Risse, Y. Lu, H. Markötter and I. Manke, *ACS Energy Lett.*, 2018, **3**, 356–365.

This journal is © The Royal Society of Chemistry 2023

Energy Environ. Sci., 2023, **16**, 2591–2602 | **2601**

48 F. Li, J. He, J. Liu, M. Wu, Y. Hou, H. Wang, S. Qi, Q. Liu, J. Hu and J. Ma, *Angew. Chem., Int. Ed.*, 2021, **60**, 6600–6608.

49 M. Tao, Y. Xiang, D. Zhao, P. Shan, Y. Sun and Y. Yang, *Nano Lett.*, 2022, **22**, 6775–6781.

50 M. J. Zachman, Z. Tu, S. Choudhury, L. A. Archer and L. F. Kourkoutis, *Nature*, 2018, **560**, 345–349.

51 C. Gong, S. D. Pu, X. P. Gao, S. Yang, J. Liu, Z. Ning, G. J. Rees, I. Capone, L. Pi, B. Liu, G. O. Hartley, J. Fawdon, J. Luo, M. Pasta, C. R. M. Grovenor, P. G. Bruce and A. W. Robertson, *Adv. Energy Mater.*, 2021, **11**, 2003118.

52 G. Xu, J. Li, C. Wang, X. Du, D. Lu, B. Xie, X. Wang, C. Lu, H. Liu, S. Dong, G. Cui and L. Chen, *Angew. Chem., Int. Ed.*, 2021, **60**, 7770–7776.

53 W. Xue, M. Huang, Y. Li, Y. G. Zhu, R. Gao, X. Xiao, W. Zhang, S. Li, G. Xu, Y. Yu, P. Li, J. Lopez, D. Yu, Y. Dong, W. Fan, Z. Shi, R. Xiong, C. J. Sun, I. Hwang, W. K. Lee, Y. Shao-Horn, J. A. Johnson and J. Li, *Nat. Energy*, 2021, **6**, 495–505.

54 C. Mitra, Z. Hu, P. Raychaudhuri, S. Wirth, S. I. Csiszar, H. H. Hsieh, H. J. Lin, C. T. Chen and L. H. Tjeng, *Phys. Rev. B: Condens. Matter Mater. Phys.*, 2003, **67**, 092404.

55 A. N. Vasiliev, O. S. Volkova, L. S. Lobanovskii, I. O. Troyanchuk, Z. Hu, L. H. Tjeng, D. I. Khomskii, H. J. Lin, C. T. Chen, N. Tristan, F. Kretzschmar, R. Klingeler and B. Büchner, *Phys. Rev. B: Condens. Matter Mater. Phys.*, 2008, **77**, 104442.

56 T. Burnus, Z. Hu, H. H. Hsieh, V. L. J. Joly, P. A. Joy, M. W. Haverkort, H. Wu, A. Tanaka, H. J. Lin, C. T. Chen and L. H. Tjeng, *Phys. Rev. B: Condens. Matter Mater. Phys.*, 2008, **77**, 125124.

57 T. Burnus, Z. Hu, H. Wu, J. C. Cezar, S. Niitaka, H. Takagi, C. F. Chang, N. B. Brookes, H. J. Lin, L. Y. Jang, A. Tanaka, K. S. Liang, C. T. Chen and L. H. Tjeng, *Phys. Rev. B: Condens. Matter Mater. Phys.*, 2008, **77**, 205111.

58 N. Hollmann, Z. Hu, M. Valldor, A. Maignan, A. Tanaka, H. H. Hsieh, H. J. Lin, C. T. Chen and L. H. Tjeng, *Phys. Rev. B: Condens. Matter Mater. Phys.*, 2009, **80**, 085111.

59 J. M. Chen, Y. Y. Chin, M. Valldor, Z. Hu, J. M. Lee, S. C. Haw, N. Hiraoka, H. Ishii, C. W. Pao, K. D. Tsuei, J. F. Lee, H. J. Lin, L. Y. Jang, A. Tanaka, C. T. Chen and L. H. Tjeng, *J. Am. Chem. Soc.*, 2014, **136**, 1514–1519.

60 S. Agrestini, C.-Y. Kuo, D. Mikhailova, K. Chen, P. Ohresser, T. W. Pi, H. Guo, A. C. Komarek, A. Tanaka, Z. Hu and L. H. Tjeng, *Phys. Rev. B*, 2017, **95**, 245131.

61 J. Zhou, L. Zhang, Y. C. Huang, C. L. Dong, H. J. Lin, C. T. Chen, L. H. Tjeng and Z. Hu, *Nat. Commun.*, 2020, **11**, 1–10.

62 X. Zhong, M. Oubla, X. Wang, Y. Huang, H. Zeng, S. Wang, K. Liu, J. Zhou, L. He, H. Zhong, N. Alonso-Vante, C. W. Wang, W. B. Wu, H. J. Lin, C. T. Chen, Z. Hu, Y. Huang and J. Ma, *Nat. Commun.*, 2021, **12**, 1–12.

63 G. Chen, Z. Hu, Y. Zhu, Z. G. Chen, Y. Zhong, H. J. Lin, C. T. Chen, L. H. Tjeng, W. Zhou and Z. Shao, *J. Mater. Chem. A*, 2018, **6**, 9854–9859.

64 L. H. Tjeng, C. T. Chen and S. W. Cheong, *Phys. Rev. B: Condens. Matter Mater. Phys.*, 1992, **45**, 8205–8208.

65 E. Pellegrin, L. H. Tjenga, F. M. F. de Groota, R. Hespera, G. A. Sawatzkya, Y. Moritomo and Y. Tokurab, *J. Electron Spectrosc. Relat. Phenom.*, 1997, **86**, 115–118.

66 Y. Y. Chin, Z. Hu, H. J. Lin, S. Agrestini, J. Weinen, C. Martin, S. Hébert, A. Maignan, A. Tanaka, J. C. Cezar, N. B. Brookes, Y. F. Liao, K. D. Tsuei, C. T. Chen, D. I. Khomskii and L. H. Tjeng, *Phys. Rev. B*, 2019, **100**, 205139.

67 C. Liang, L. Jiang, Z. Wei, W. Zhang, Q. Wang and J. Sun, *J. Energy Chem.*, 2022, **65**, 424–432.

68 D. Lu, G. Xu, Z. Hu, Z. Cui, X. Wang, J. Li, L. Huang, X. Du, Y. Wang, J. Ma, X. Lu, H. J. Lin, C. T. Chen, A. A. Nugroho, L. H. Tjeng and G. Cui, *Small Methods*, 2019, **3**, 1900546.

2602 | *Energy Environ. Sci.*, 2023, **16**, 2591–2602

This journal is © The Royal Society of Chemistry 2023